Mon. Not. R. Astron. Soc. **000**, 000–000 (0000) Printed 26 June 2017 (MN LATEX style file v2.2)

MOVES I. The evolving magnetic field of the planet-hosting star HD189733

R. Fares[1,2⋆], V. Bourrier[3], A.A. Vidotto[3,4], C. Moutou[5,6], M.M. Jardine[7], P. Zarka[8] Ch. Helling[9], A. Lecavelier des Etangs[10], J. Llama[11], T. Louden[12], P.J. Wheatley[12] D. Ehrenreich[3]

[1] *INAF - Osservatorio Astrofisico di Catania, Via Santa Sofia 78, 95123 Catania, Italy*
[2] *Department of Natural Sciences, School of Arts and Sciences, Lebanese American University, P.O. Box 36, Byblos, Lebanon*
[3] *Observatoire de l'Université de Genève, Chemin des Maillettes 51, Versoix, CH-1290, Switzerland*
[4] *School of Physics, Trinity College Dublin, Dublin-2, Ireland*
[5] *LAM–UMR 6110, CNRS & Univ. de Provence, 38 rue Fréderic Juliot-Curie, F–13013 Marseille, France*
[6] *CFHT, 65-1238 Mamalahoa Hwy., Kamuela, HI 96743, USA*
[7] *SUPA, School of Physics and Astronomy, Univ. of St Andrews, St Andrews, Scotland KY16 9SS, UK*
[8] *LESIA, Observatoire de Paris, CNRS, PSL/SU/UPMC/UPD/SPC, Place J. Janssen, 92195 Meudon, France*
[9] *Centre for Exoplanet Science, SUPA, School of Physics and Astronomy, Univ. of St Andrews, St Andrews, Scotland KY16 9SS, UK*
[10] *IAP-UMR7095, CNRS & Université Pierre & Marie Curie, 98bis boulevard Arago, 75014 Paris, France*
[11] *Lowell Observatory, 1400 W. Mars Hill Rd. Flagstaff. Arizona, 86001, USA*
[12] *Department of Physics, University of Warwick, Coventry CV4 7AL, UK*

ABSTRACT

HD189733 is an active K dwarf that is, with its transiting hot Jupiter, among the most studied exoplanetary systems. In this first paper of the Multiwavelength Observations of an eVaporating Exoplanet and its Star (MOVES) program, we present a 2-year monitoring of the large-scale magnetic field of HD189733. The magnetic maps are reconstructed for five epochs of observations, namely June-July 2013, August 2013, September 2013, September 2014, and July 2015, using Zeeman-Doppler Imaging. We show that the field evolves along the five epochs, with mean values of the total magnetic field of 36, 41, 42, 32 and 37 G, respectively. All epochs show a toroidally-dominated field. Using previously published data of Moutou et al. (2007) and Fares et al. (2010), we are able to study the evolution of the magnetic field over 9 years, one of the longest monitoring campaign for a given star. While the field evolved during the observed epochs, no polarity switch of the poles was observed. We calculate the stellar magnetic field value at the position of the planet using the Potential Field Source Surface extrapolation technique. We show that the planetary magnetic environment is not homogeneous over the orbit, and that it varies between observing epochs, due to the evolution of the stellar magnetic field. This result underlines the importance of contemporaneous multi-wavelength observations to characterise exoplanetary systems. Our reconstructed maps are a crucial input for the interpretation and modelling of our MOVES multi-wavelength observations.

Key words: stars: magnetic fields – stars: individual: HD189733 – techniques: polarimetry – Planet-Star Interaction

1 INTRODUCTION

Hot-Jupiters (HJs), i.e., gas giant exoplanets orbiting close ($\lesssim 0.1$ au) to their host stars, are useful laboratories to study the complex interactions (e.g. magnetospheric, tidal, ionisation) between exoplanets and their host-stars. Because of the short orbital distance of HJs, interactions are expected to be strong and could potentially be detected with current instrumentation. The high stellar XUV fluxes that HJs are subjected to can lead to enhanced heating and atmospheric escape (e.g., Lecavelier Des Etangs 2007; Murray-Clay, Chiang & Murray 2009; Davis & Wheatley 2009; Lammer et al. 2011; Jackson, Davis & Wheatley 2012; Bourrier & Lecave-

⋆ E-mail: rfares@oact.inaf.it

lier des Etangs 2013; Koskinen et al. 2013), which can be probed through transmission spectroscopy technique (Vidal-Madjar et al. 2003; Fossati et al. 2010; Lecavelier Des Etangs et al. 2010; Ehrenreich et al. 2012; Lecavelier des Etangs et al. 2012; Bourrier et al. 2013). In addition to the extreme radiation environment, HJs are also immersed in stellar winds, whose physical characteristics are unparalleled to those felt by the planets in our own solar system (Preusse et al. 2005; Grießmeier et al. 2007; Vidotto et al. 2009, 2015). The extreme particle and magnetic environments of the stellar wind could lead to powerful reconnection events between the stellar and planetary magnetospheres (e.g. Ip, Kopp & Hu 2004), which may have the potential to enhance the stellar activity (Cuntz, Saar & Musielak 2000; Shkolnik, Walker & Bohlender 2003; Shkolnik et al. 2008; Scandariato et al. 2013). In addition, as a result of the interaction between the planet's magnetosphere and the coronal material of the star, bow shocks might also form around HJs (e.g. Vidotto, Jardine & Helling 2010; Cohen et al. 2011; Llama et al. 2013; Matsakos, Uribe & Königl 2015), explaining asymmetric UV transit features (Fossati et al. 2010; Vidotto, Jardine & Helling 2010). Radio emission resultant from the interaction between the stellar magnetised wind and a magnetised exoplanet is expected to be several orders of magnitude larger than that of the largest emitter in our own solar system, Jupiter (Zarka 2007; Grießmeier, Zarka & Spreeuw 2007; Jardine & Cameron 2008; Fares et al. 2010; Vidotto et al. 2012, 2015; See et al. 2015). A varying stellar magnetic field has also implication for the atmosphere of the orbiting planet leading to variability of the Cosmic Ray flux reaching the planetary atmosphere (Helling et al. 2013; Rimmer & Helling 2013). Cosmic rays have been studied as one example for external ionisation sources that also effect the chemical compositions by possibly opening reaction paths to carbo-hydrate molecules (Rimmer, Stark & Helling 2014; Rimmer, Helling & Bilger 2014).

HD189733 is an ideal system to study these different types of interactions. At a distance of 19.3 pc, the bright (V=7.7) and active K2V star hosts a transiting HJ orbiting at 0.031 ± 0.001 au, i.e., at an orbital distance of 8.84 ± 0.27 $R_\star$ (see Table 1). The interactions within this system have been the subject of many studies in the literature (e.g. Smith et al. 2009; Pillitteri et al. 2010; Berdyugina et al. 2011; Lecavelier Des Etangs et al. 2011; Ben-Jaffel & Ballester 2013; Bourrier & Lecavelier des Etangs 2013; Bourrier et al. 2013; Poppenhaeger, Schmitt & Wolk 2013; Louden & Wheatley 2015; Brogi et al. 2016; Bott et al. 2016; Barnes et al. 2016). Because of its active host, HD189733b is in fast-changing radiation, particle and magnetic environments. Recent UV observations of the planetary transit showed that the properties of the hydrogen exosphere surrounding the planet are varying over time (Lecavelier des Etangs et al. 2012). An X-ray flare was detected 8h prior to the UV detection of atmospheric escape, suggesting that variations in the XUV emission of the host-star and/or its magnetised outflowing plasma might have been the cause of the observed variability.

Variations in the quiescent stellar wind are also expected for this system. Through spectropolarimetric observations performed by Moutou et al. (2007) and Fares et al. (2010), it was shown that the large-scale magnetic field of HD189733 varied for the observed epochs. Recently, using the large-scale magnetic maps reconstructed by Fares et al. (2010), Llama et al. (2013) showed that the stellar wind of HD189733 presents inhomogeneities at the position of the planet, which could cause short timescale variations in the UV transit lightcurve (on the order of an orbital period), as well as longer timescale variations (on the order of a year, due to the change in the stellar magnetic field). These authors concluded that multi-wavelength data acquired simultaneously would provide the best tool for a comprehensive characterisation of the system.

Table 1. Summary of the physical properties of HD189733 and its hot Jupiter, HD189733b.

Physical property	value	reference
Star:		
Sp. type	K2V	
V (mag)	7.7	
$T_{\rm eff}$ (K)	5050 ± 50	Bouchy et al. (2005)
$M_\star (M_\odot)$	0.92 ± 0.03	Bouchy et al. (2005)
$R_\star (R_\odot)$	0.76 ± 0.01	Winn et al. (2007)
$v \sin i$ (km s^{-1})	2.97 ± 0.22	Winn et al. (2006)
$P_{\rm rot}$ (d)	11.94 ± 0.16	Fares et al. (2010)
$i_\star (^\circ)$	~ 85	Fares et al. (2010)
$d\Omega$ (rad s^{-1})	0.146 ± 0.049	Fares et al. (2010)
Planet:		
$i_{\rm orb} (^\circ)$	85.76 ± 0.29	Boisse et al. (2009)
$M_p (M_{\rm Jup})$	1.13 ± 0.03	Boisse et al. (2009)
$R_p (R_{\rm Jup})$	1.154 ± 0.032	Boisse et al. (2009)
$P_{\rm orb} (d)$	2.2185733 ± 0.0000019	Boisse et al. (2009)
a (au)	0.031 ± 0.001	Boisse et al. (2009)
$i_{\rm spin-orbit}$	$0.85^{+0.32}_{-0.28}$	Triaud et al. (2009)

In this context, we started a multi-wavelength observational campaign of this system, in the frame of the MOVES collaboration (Multiwavelength Observations of an eVaporating Exoplanet and its Star, PI V. Bourrier). Observations of the star and the planet were obtained at similar epochs with ground-based and space-borne instruments in X-rays with Swift and XMM-Newton, UV with HST and XMM-Newton, optical spectropolarimetry with NARVAL and ESPaDOnS, and radio with LOFAR. In the present (first) paper of this collaboration, we use optical spectropolarimetric observations to reconstruct the surface magnetic field of HD189733 at five different epochs, contemporaneous to other sets of observations. These magnetic field maps will provide a crucial input to the analysis, modelling and interpretation of the multi-wavelength data sets that will follow in forthcoming papers.

This paper is organised as follows. Section 2 presents our observations. In Section 3, we describe the magnetic imaging method we use. The results are shown in Section 4, where we present the reconstruction of the magnetic field of HD189733 at five different epochs. We discuss the magnetic field evolution of HD189733 in Section 5, based on this paper's results and results of Moutou et al. (2007) and Fares et al. (2010). Section 6 presents the summary and conclusions of this work.

2 OBSERVATIONS

Our spectropolarimetric data were obtained using both NARVAL spectropolarimeter at the TBL (2m) and ESPaDOnS at CFHT (3.6m). A spectropolarimeter is a spectrograph with a polarisation section, allowing measurement of the polarisation of the spectral lines. A circular polarisation spectrum is extracted from 4 subexposures taken each at a different angle of the polarisation waveplates. ESPaDOns and NARVAL are twin instruments, both operating in the optical domain (370 to 1000 nm) at a resolution of 65,000 in the polarisation mode. Data reduction is done automatically using Libre-Esprit, a fully automated reduction tool installed at TBL and CFHT (Donati et al. 1997). The spectra are normalised to a unit continuum, their wavelengths referring to the Heliocentric rest frame. Telluric lines are used to correct from spectral shifts due to instrumental effects. This correction secures a radial velocity (RV) precision of about 15 $\mathrm{m\,s^{-1}}$ (Moutou et al. 2007; Morin et al. 2008b).

Observations with both NARVAL and ESPaDOnS were obtained in service mode. Our NARVAL 2013 data (PI Bourrier) were collected as follow: 5 spectra in May (11-13), 2 spectra in June (12-15), 5 spectra in July (01-04-05-08-14), 14 spectra in August (02 to 23), 13 spectra in September (02 to 24) and finally 5 spectra in October (08-09-12-13-18). ESPaDOnS' data were obtained via a filling program targeting planet-hosting stars (PI Moutou), 7 spectra were collected in September 2013. Table 2 presents the log of observations of all our data in 2013. In 2014, 15 spectra were collected between 01 September and 20 October. Another 18 spectra were collected between 20 May 2015 and 20 July 2015. The log of the 2014 and the 2015 (PI Bourrier) observations are presented in Table 3.

The equatorial rotation period of HD189733 is $\sim$ 12 days (Fares et al. 2010). For the sake of homogeneity with our previous studies of this star, we used the same ephemeris as in Moutou et al. (2007) and Fares et al. (2010). Rotational ($\mathrm{E_{Rot}}$) and orbital ($\mathrm{E_{Orb}}$) cycles are calculated by:

$$\begin{aligned} T_0 &= \mathrm{HJD}\ 2,453,629.389 + 12\ \mathrm{E_{Rot}} \\ T_0 &= \mathrm{HJD}\ 2,453,629.389 + 2.218575\ \mathrm{E_{Orb}} \end{aligned} \quad (1)$$

For cool stars, the polarisation signature in single lines is typically within the noise level. Using the polarisation information of many spectral line simultaneously, we can extract the polarisation signal of the spectrum, this is known as multi-line technique Least-Square Deconvolution (LSD, Donati et al. 1997). LSD assumes that all lines have the same polarisation information, and extracts the polarisation signature by deconvolving the observed spectrum with a line mask. LSD calculates intensity (Stokes I) profiles, circular polarisation (Stokes V) profiles, as well as a null polarisation profiles (labelled N). These profiles are calculated using a combination of the sub-exposures taken at different angles of the waveplates. The Null profile is a check profile, it is calculated such to cancel out the stellar polarisation signature, and thus should contain no polarisation. It helps check for spurious or instrumental signatures. For more details on how these profiles are calculated, see Donati et al. (1997) and Mengel et al. (2017).

We compute a line mask for HD 189733 using Kurucz's lists of atomic line parameters (Kurucz CD-Rom 18) and a Kurucz model atmosphere with solar abundances, temperature set to 5000 K and logarithmic gravity (in $\mathrm{cm\,s^{-2}}$) set to 4.0. Only moderate-to-strong lines, featuring central depths larger than 40% of the local continuum, are included in the mask (before any macroturbulent or rotational broadening); the strongest and broadest features (such as Balmer lines) are excluded. In the optical domain, this mask contains about 4000 lines. The LSD profiles calculated by deconvolving the stellar spectra with the mask have a S/N $\sim$ 30 times higher than the S/N in single lines with average magnetic sensitivity (see Tables 2 and 3), allowing for the detection of the polarisation signature.

We calculated the RV of each Stokes I profile by fitting a Gaussian profile to it. Since the star hosts a hot-Jupiter, the RV signatures varies over the planetary orbit. Our RV data agree (within the error bars) with the orbital solution of Boisse et al. (2009). There is an offset between our values and theirs, $+0.06\ \mathrm{km\,s^{-1}}$ for June-July 2013, $+0.13\ \mathrm{km\,s^{-1}}$ for August 2013, $+0.10\ \mathrm{km\,s^{-1}}$ for September 2013, $+0.13\ \mathrm{km\,s^{-1}}$ for September 2014, and $+0.11\ \mathrm{km\,s^{-1}}$ for June 2015. Such offsets are due to the use of different reduction pipelines (ESPaDOnS and Narval vs Sophie). For the tomographic Imaging, we shift each profile by its RV to centre all profiles around 0 $\mathrm{km\,s^{-1}}$.

3 MODEL DESCRIPTION AND IMAGING METHOD

Magnetic fields, when present in the photosphere, cause splitting of the magnetically sensitive spectral lines via the Zeeman effect. The lines that form in such environments are polarised. Measuring the wavelength shift between spectral components of the line (when possible, which depends, among others, on the amplitude of this shift, the rotational broadening and the spectrograph resolution) allows us to calculate the longitudinal magnetic field of the star (see, e.g., Shulyak et al. (2014) for M dwarfs). The field topology (i.e. distribution, polarity, configuration), on the other hand, can not be determined by the wavelength shift alone, but is determined using a tomographic imaging technique, Zeeman-Doppler Imaging ZDI (Donati et al. 1997). Polarisation of the spectral lines depends on the orientation of the magnetic field relative to the line of sight (see Fig 2 of Reiners 2012). To map the field, spectra are collected during one or more stellar rotations. ZDI inverts these spectra/profiles into a magnetic topology that can produce the observed polarisation signatures. Because this problem is ill-posed, ZDI uses Maximum-Entropy regularisation to get the simplest magnetic map compatible with the data.

In the newest version of ZDI (Donati et al. 2006), the field is described by its poloidal and toroidal components (Chandrasekhar 1961), with all the components expressed in terms of spherical harmonics expansion. The highest degree of spherical harmonic expansion used to map the field represents the ZDI map resolution around the equator. For slow rotators, such as HD189733, we limit the spherical harmonics to the lowest degrees ($l \leq 5$, see Fares et al. 2010 for more details). ZDI follows an iterative procedure, it compares synthetic Stokes V profiles to the observed profiles col-

Table 2. List of observations in 2013. The columns list, respectively, the dates of observation, Heliocentric Julian Date and UT time of observations (at mid-exposure), the peak S/N (per 2.6 $\mathrm{km\,s^{-1}}$ velocity bin) of each observation (around 700 nm), the rotational cycle of the star and orbital cycle of the planet calculated using the ephemeris of Eq. 1, and the radial velocity (RV) of the star at each exposure, the rms noise level (relative to the unpolarized continuum level I_c and per 1.8 $\mathrm{km\,s^{-1}}$ velocity bin) in the circular polarisation profile produced by LSD. The data were taken using NARVAL spectropolarimeter, except for 6 spectra collected using ESPaDOnS (marked by * next to the date of observation). The exposure time of each observation is 4×900 s. Dates marked with † were not used for the mapping of the stellar field (see text for more details).

Date (UT) (2013)	HJD (2,456,000+)	UT (h:m:s)	S/N	Rot. Cycle (239+)	Orb. Cycle (1297+)	$v_{\rm rad}$ ($\mathrm{km\,s^{-1}}$)	σ_{LSD} ($10^{-4}I_c$)
12 May†	424.58158	01:55:55	630	-6.0673	-37.0955	-2.134	0.50
12 May†	424.62595	02:59:48	670	-6.0636	-37.0755	-2.154	0.48
13 May†	425.59553	02:15:52	680	-5.9828	-36.6385	-2.340	0.46
13 May†	425.63991	03:19:46	680	-5.9791	-36.6185	-2.325	0.46
14 May†	426.62177	02:53:31	660	-5.8973	-36.1759	-2.029	0.47
13 Jun	456.53057	00:38:37	440	-3.4049	-22.6948	-2.385	0.81
16 Jun	459.52985	00:37:17	540	-3.1549	-21.3429	-2.045	0.62
02 Jul	475.60489	02:24:02	650	-1.8153	-14.0973	-2.075	0.51
05 Jul	478.60456	02:23:22	650	-1.5654	-12.7452	-2.477	0.47
06 Jul	479.59405	02:08:10	580	-1.4829	-12.2992	-2.045	0.56
08 Jul	482.52265	24:25:11	690	-1.2389	-10.9792	-2.218	0.47
15 Jul	488.54927	01:03:14	380	-0.7366	-8.2627	-1.906	0.92
02 Aug	507.50215	23:55:01	400	0.8428	0.2801	-2.298	0.87
04 Aug	509.37413	20:50:4	660	0.9988	1.1239	-2.277	0.50
05 Aug	510.51950	24:20:01	440	1.0942	1.6401	-2.00	0.71
08 Aug	513.50839	24:04:03	530	1.3433	2.9873	-2.124	0.63
09 Aug	514.50144	23:54:04	680	1.426	3.4349	-2.241	0.46
10 Aug	515.50391	23:57:39	650	1.5096	3.8868	-2.016	0.49
11 Aug	516.52369	24:26:09	660	1.5946	4.3464	-2.294	0.49
14 Aug	518.53989	0:49:32	680	1.7626	5.2552	-2.326	0.46
15 Aug	520.38524	21:06:53	530	1.9164	6.0870	-2.268	0.59
18 Aug	523.37830	20:56:59	630	2.1658	7.4361	-2.225	0.51
19 Aug	524.46529	23: 2:18	670	2.2564	7.926	-2.058	0.47
21 Aug	526.49842	23:50:05	610	2.4258	8.8425	-2.027	0.53
22 Aug	527.40235	21:31:48	650	2.5011	9.2499	-2.37	0.50
23 Aug	528.50256	23:56:09	640	2.5928	9.7458	-1.938	0.51
02 Sep	538.34180	20:05:15	680	3.4127	14.1807	-2.352	0.47
03 Sep	539.40804	21:40:42	660	3.5016	14.6613	-1.985	0.47
04 Sep	540.37393	20:51:39	650	3.5821	15.0967	-2.287	0.51
08 Sep	544.47392	23:15:58	610	3.9237	16.9447	-2.125	0.53
10 Sep	546.42285	22: 2:36	670	4.0862	17.8232	-2.014	0.48
11 Sep	547.39768	21:26:26	660	4.1674	18.2626	-2.387	0.48
12 Sep	548.39552	21:23:24	660	4.2505	18.7123	-2.082	0.30
13 Sep*	548.86339	08:37:12	1020	4.2895	18.9232	-2.082	0.30
13 Sep	549.40705	21:40:06	560	4.3348	19.1683	-2.346	0.60
15 Sep	551.36003	20:32:34	420	4.4976	20.0486	-2.211	0.76
17 Sep*	552.89635	09:25:02	900	4.6256	20.7410	-1.986	0.37
19 Sep	555.38839	21:13:48	670	4.8333	21.8643	-2.242	0.34
20 Sep*	555.73218	05:28:55	960	4.8619	22.0193	-2.242	0.34
20 Sep	556.39231	21:19:33	640	4.9169	22.3168	-2.39	0.49
21 Sep	557.35420	20:24:46	560	4.9971	22.7504	-2.183	0.34
22 Sep*	557.88116	09:03:4	990	5.0410	22.9879	-2.182	0.34
24 Sep*†	559.89429	09:22:47	870	5.2088	23.8953	-2.017	0.39
24 Sep	560.32644	19:45:07	670	5.2448	24.0901	-2.36	0.33
25 Sep*	560.80689	07:17:02	970	5.2848	24.3066	-2.36	0.33
27 Sep*	562.89300	09:21:16	880	5.4587	25.2469	-2.379	0.37
08 Oct†	574.28920	18:53:07	690	6.4084	30.3837	-2.332	0.46
09 Oct†	575.28808	18:51:38	670	6.4916	30.8339	-2.007	0.47
12 Oct†	578.28726	18:50:50	610	6.7415	32.1857	-2.329	0.53
13 Oct†	579.29042	18:55:31	530	6.8251	32.6379	-2.008	0.63
18 Oct†	584.28323	18:45:50	560	7.2412	34.8884	-2.037	0.60

Table 3. Same as Table 2 for the observations in 2014 and 2015. The exposure time is 4×900 s, expect for 28 May 2015 with an exposure time of 4×800 s, and 20 July 2015 where only two sub-exposures of 900 s each were taken. All spectra were obtained using NARVAL. Dates marked with † were not used for the mapping of the stellar field.

Date (UT)	HJD (2,456,000+)	UT (h:m:s)	S/N	Rot. Cycle (239+)	Orb. Cycle (1297+)	$v_{\rm rad}$ (km s^{-1})	σ_{LSD} ($10^{-4} I_{\rm c}$)
01 Sep 2014	902.40942	21:42:33	690	33.7517	178.2805	-2.339	0.47
02 Sep 2014	903.37339	20:50:43	660	33.8320	178.7150	-1.966	0.49
03 Sep 2014	904.37260	20:49:39	670	33.9153	179.1654	-2.312	0.48
05 Sep 2014	906.37382	20:51:33	680	34.0821	180.0674	-2.193	0.46
10 Sep 2014	911.37147	20:48:35	670	34.4985	182.3200	-2.338	0.48
11 Sep 2014	912.35651	20:27:07	640	34.5806	182.7640	-1.948	0.51
12 Sep 2014	913.39844	21:27:35	660	34.6675	183.2337	-2.366	0.50
24 Sep 2014†	925.34813	20:16:19	90	35.6633	188.6199	-2.041	5.20
25 Sep 2014	926.34560	20:12:47	460	35.7464	189.0695	-2.260	0.71
26 Sep 2014	927.34206	20:07:48	600	35.8294	189.5186	-2.105	0.55
27 Sep 2014	928.33867	20:03:01	560	35.9125	189.9678	-2.092	0.59
15 Oct 2014†	946.31976	19:37:60	320	37.4109	198.0726	-2.197	1.13
19 Oct 2014†	950.32639	19:48: 5	110	37.7448	199.8786	-2.032	3.92
20 Oct 2014†	951.31730	19:35: 8	660	37.8274	200.3252	-2.303	0.48
26 Oct 2014†	957.27473	18:34:38	600	38.3238	203.0105	-2.219	0.56
28 May 2015†	1170.62294	02:53:29	550	56.1028	299.1750	-2.392	0.61
29 May 2015†	1171.55663	01:17:53	530	56.1806	299.5958	-2.077	0.64
31 May 2015†	3173.55224	01:11:19	590	56.3469	300.4953	-2.193	0.56
08 June 2015†	1181.58663	01:59:55	510	57.0165	304.1168	-2.331	0.64
25 June 2015	1199.48188	23:27:23	600	58.5077	312.1829	-2.459	0.56
30 June 2015	1203.56315	01:24:06	560	58.8478	314.0225	-2.207	0.64
01 July 2015	1204.53004	00:36:21	570	58.9284	314.4583	-2.259	0.61
06 July 2015	3210.48886	23:36:40	560	59.4250	317.1442	-2.351	0.59
07 July 2015	3211.48835	23:35:53	600	59.5083	317.5947	-2.059	0.55
08 July 2015	3212.49073	23:39:15	580	59.5918	318.0465	-2.241	0.53
09 July 2015	1213.47407	23:15:13	670	59.6738	318.4897	-2.179	0.48
10 July 2015	1214.49616	23:46:58	530	59.7589	318.9504	-2.087	0.54
12 July 2015	1215.52747	00:31:60	610	59.8449	319.4153	-2.251	0.54
12 July 2015	1216.51175	24:09:19	550	59.9269	319.8589	-1.991	0.60
13 July 2015	1217.52512	24:28:31	670	60.0113	320.3157	-2.364	0.50
14 July 2015	1218.52267	24:24:57	570	60.0945	320.7653	-1.974	0.59
16 July 2015	1219.52866	00:33:32	430	60.1783	321.2187	-2.337	0.79
20 July 2015	1224.42541	22:04:41	360	60.5864	323.4259	-2.170	0.86

lected during the stellar rotational cycles. In practice, the stellar surface is divided into 9000 grid cells of similar area. The contribution of each grid cell is then calculated in the weak field regime, and a synthetic Stokes profile for each observed rotation phase is produced.

In addition to the field intensity and distribution, ZDI also gives an indication on the stellar inclination (up to $\sim 10^\circ$ accuracy), on the stellar rotation period (see, e.g. Alvarado-Gómez et al. 2015), and on the differential rotation (DR). We describe DR using a solar-like DR law, where the rotation rate at a latitude θ is defined by $\Omega(\theta) = \Omega_{\rm eq} - d\Omega \sin^2(\theta)$, where $\Omega_{\rm eq}$ and $d\Omega$ are respectively the rotation rate at the equator, and the difference in rotation rate between the pole and the equator. In practice, to measure DR, we reconstruct the magnetic image at a given magnetic energy for a pair of fixed ($\Omega_{\rm eq}$, $d\Omega$), and obtain the reduced-chi squared ($\chi^2_{\rm r}$) of the fit. We investigate the $\chi^2_{\rm r}$ values of the 2D parameter space of ($\Omega_{\rm eq}$, $d\Omega$). The optimum DR parameters are the ones minimizing $\chi^2_{\rm r}$. They are obtained by fitting the surface of the $\chi^2_{\rm r}$ map with a paraboloid around the minimum value of $\chi^2_{\rm r}$.

The Null profiles, for each epoch, are used as a test to check for spurious polarisation. In practice, we fit these profiles with a zero magnetic field configuration. Since the Null profiles should contain no polarisation, the $\chi^2_{\rm r}$ of the fit should be one or less. A $\chi^2_{\rm r}$ greater than one indicates either a spurious polarisation signature, or an underestimation of the error bars. If a systematic signature is found in the profiles, it indicates a spurious origin of the signature. We calculate a mean signature of the Null profiles, and subtract it from the Stokes V profiles to eliminate this spurious feature.

4 RESULTS

ZDI requires the use of data covering one or more stellar rotations to derive the photospheric magnetic map. In some field configurations (see, e.g. Morin et al. 2008a) the large-scale magnetic field of the star is stable for many stellar rotations, and also over many years. In these cases, one can combine data collected over many rotations together as one dataset. To estimate whether the field is stable over

many stellar rotations, we compare the quality of the fit and the shape of the polarisation profiles at the same rotational phases.

Our observations cover many stellar rotations at each observing epoch, from June 2013 to July 2015 (see Tables 2 and 3).

We performed a series of tests on the data, reconstructing the maps using a combination of datasets for each epoch. We find that using Stokes V profiles spread over more than two consecutive stellar rotations to reconstruct the map worsens the quality of the fit. We therefore adopted datasets of up to two stellar rotations for each reconstructed map. Some spectra were not used in the reconstruction because they were collected with a rotational phase gap of more than a stellar rotation in respect to the main dataset (see Tables 2 and 3).

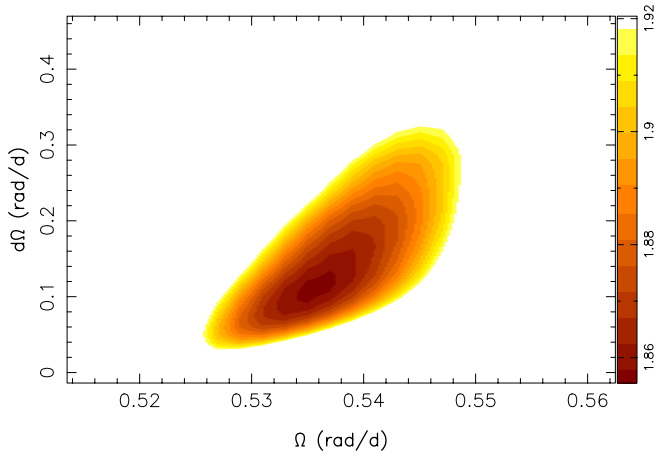

Figure 1. Variations of χ^2_r as a function of Ω_{eq} and $d\Omega$, derived from the modelling of the Stokes V data set for August 2013. The outer colour contour corresponds to a 3.5% increase in the χ^2_r , and traces a 3 σ interval for both parameters taken as a pair.

4.1 Differential rotation

Differential rotation distorts the magnetic regions on the stellar surface. Spectropolarimetric data can therefore be used to estimate the level of DR.

We applied the same technique as in Fares et al. (2010) to search for differential rotation in our data (explained in Section 3). In this study, we were able to detect DR for August 2013 dataset. The χ^2_r map in the (Ω_{eq}, $d\Omega$) space is shown in Fig 1. A well defined χ^2_r minimum is found for $d\Omega = 0.11 \pm 0.05$ rad d^{-1} and Ω_{eq} of 0.535 ± 0.004 rad d^{-1}, corresponding to a rotation period at the equator 11.7$\pm$0.1d. The shear value $d\Omega$ is consistent with the one measured by Fares et al. (2010) at $d\Omega = 0.146 \pm 0.049$ rad d^{-1}. These measurements, within their uncertainties, do not reveal a variation of DR.

HD 189733 is a slow rotator for which the Fourier Transform of the Intensity profile technique presented by Reiners & Schmitt (2002) can not be applied. There are no measurements of the DR of this star in the literature, apart from the recent work of Cegla et al. (2016). Cegla et al. (2016) modelled the Rossiter-McLaughlin effect to probe planetary parameters and stellar differential rotation, and found a $d\Omega > 0.12$ rad d^{-1} for HD 189733, in agreement with our findings.

Stellar differential rotation is not constant across spectral types and rotation rates. Many observational and theoretical studies have addressed the question of its variation (see, e.g., Barnes et al. 2005; Reiners 2006; Collier Cameron 2007; Augustson et al. 2012; Reinhold, Reiners & Basri 2013; Distefano et al. 2016; Balona & Abedigamba 2016). Using Kepler photometric data, Reinhold, Reiners & Basri (2013) and Balona & Abedigamba (2016) studied the DR for a large sample of stars. HD 189733 DR is within the range of the shear values of Kepler stars both as a function of temperature and as a function of rotation. Balona & Abedigamba (2016) propose an empirical relation between the shear value, the effective temperature of the star and its rotation. For HD 189733, the predicted value of the $d\Omega$ is $0.076^{+0.004}_{-0.001}$. Our value is slightly higher, their value is, however, within the error bars of our measurement.

4.2 Magnetic maps

We reconstruct the magnetic maps for five observing epochs. The observed Stokes V (in red) and a 1-sigma error-bar are shown in Fig 2, along with the ZDI reconstructed circular polarisation (in black). The observed profiles show a detection of the polarisation signature (false-alarm probability less than 10^{-5}, see Donati et al. (1997) for the classification of the detections). The reconstructed maps are shown in Fig 3. As mentioned previously, each dataset used to reconstruct a magnetic map consisted of no more than two stellar rotations.

- June/July 2013

We reconstructed the map of June/July 2013, although our phase coverage is not optimal. The χ^2_r of the reconstruction is 1.15. The mean magnetic field is of 36 G. 61% of the magnetic energy is in the toroidal component. For the poloidal component, we define axisymetric modes as having $m = 0$ and $m<l/2$ (m and l being the order and the degree of the associated Legendre polynomial, used to describe the field as spherical harmonics expansion). About 40% of the poloidal field is axisymetric.

- August 2013

For August 2013, the data samples the stellar rotation well. However, the Null profile shows a systematic signature in the core of the profile. Fitting these Null profiles with no magnetic field configuration leads to a χ^2_r of 1.3. We calculated a mean profile for all the Null profiles. Subtracting the mean Null profile from the August 2013 Null spectra leads to a χ^2_r of 0.7 when fitting the corrected Null profiles with no magnetic configuration. Given that the signatures in the Null profiles show a systematic trend, it is more likely to be a spurious signature rather than an underestimation of the error bars. We subtract the mean Null profile signature of the Stokes V profiles. The map is reconstructed with a χ^2_r

of 1.85. The average surface magnetic field is 40 G. 50% of the total energy is in the toroidal component of the field. 2% of the poloidal energy is in the axisymetric modes, and mainly in modes with $m = 0$. The poloidal component is thus mainly non-axisymetric. Spherical harmonics modes with l>3 (i.e. modes higher than the dipole, quadrupole and octupole) contribute to $\sim$ 38% of the poloidal energy.

- September 2013

In September 2013, we have data from ESPaDOnS and NARVAL, covering two stellar rotations. We reconstructed a map using those data with a χ^2_r of 2.15. We notice a systematic difference in the Intensity profile depth between Narval's spectra and ESPaDOnS' spectra. The difference in depth is not significant enough to require different modelling of the intensity profiles between instruments. This difference is due to the normalisation of the spectra at the telescope.

The average surface magnetic field is 42 G. 59% of the energy in the toroidal component. The poloidal field is still mainly non-axisymetric (88%, see Table 4). About 50% of the poloidal component is in the octupolar mode, higher orders contribute to $\sim$ 45%.

- September 2014

In September 2014, the average magnetic field drops to 31 G (see Fig 3). The χ^2_r of the fit is 1.25. The field remains mainly toroidal, with 78% of the total energy stored in the toroidal components. The poloidal field is strongly non-axisymetric, and only 12% of the energy lies within axisymmetric modes.

- July 2015

In July 2015, the magnetic field, and in particular the radial component, has changed significantly relative to September 2014. The radial component changes polarity around the equator between September 2014 and July 2015. The poloidal component contributes to 15% of the total energy. The average magnetic field is of 37 G.

The characteristics of each reconstructed map are listed in Table 4. ZDI does not provide error bars for the reconstructed map. However, statistical errors can be calculated by varying the input parameters (e.g., $v \sin i$, stellar inclination, $\Omega_{\rm eq}$, $d\Omega$) within their error bars. Error bars on field characteristics are calculated by comparing the characteristics of the reconstructed field for the best set of input parameters to the characteristics of maps reconstructed by varying those best input parameters within their error bars. We follow Mengel et al. (2016) for error bar calculations: we fix ($\Omega_{\rm eq}$,$d\Omega$) and vary $v \sin i$ within its error bars (2.75 km s^{-1} to 3.2 km s^{-1}, Table 1). We then do a new set of maps fixing $v \sin i$ and varying ($\Omega_{\rm eq}$, $d\Omega$) within their error bars. Error bars in table 4 represent the highest values of our procedure.

4.3 Extrapolation of the magnetic field to investigate the corona and the planetary orbit

The interactions between the stellar wind and the planetary magnetosphere might trigger planetary emission, such as radio emission or bow shock formation (see, e.g. Fares et al. 2010; Llama et al. 2013), and it might influence the ionisation state of the planetary atmosphere (Rimmer & Helling 2013; Rimmer, Helling & Bilger 2014). In this Section, we examine the stellar magnetic field in the corona up to the planetary orbit using a potential field extrapolation of the surface magnetic field. For this purpose, we use the Potential Field Source surface (PFSS) code of Jardine, Collier Cameron & Donati 2002, originally developed for the Sun (van Ballegooijen et al. 1998) based on Altschuler & Newkirk (1969). The potential field extrapolation assumes that there is no electric current in the corona. The components of magnetic field in the corona are described using a spherical harmonics decomposition. This technique delivers satisfactory results when compared to wind modelling of the solar corona (Riley et al. 2006).

The PFSS model extrapolates the magnetic field considering two boundary conditions: the first one being that the field is purely radial at a surface called the Source Surface, the second boundary condition is the observed field geometry at the surface of the star. We assume that the Source Surface is at 3.4 $R_\star$. Our radial magnetic maps are used as a boundary condition at the surface of the star, thus giving a realistic model of the radial field.

The extrapolated field in the stellar corona for the five maps presented in this paper are shown in Fig 4. This figure shows how different surface field configurations produce different field line configuration in the corona. Since the magnetic field lines in the corona are not those of a very simple configuration, and since the planet and the star are not synchronised, the planet crosses different field configuration on its orbit, as well as from one orbit to the other (the planet crosses in front of the same stellar field configuration after one beat period (of rotation and orbital periods), rather than after one orbital period). We calculate, for each observing epoch, the footprints of field lines connecting the stellar surface to the position of the planet on its orbit . They are shown in Fig 5.

The PFSS model allows the calculation of the field value and orientation at each position in the corona, out to the Source Surface. Since the planet is outside the Source Surface, we proceed as follows to calculate the field at its position. First, we calculate the position of the sub-planetary point on the Source Surface, we then calculate the energy budget at this point. We remind the reader here that at the Source Surface, the stellar field is purely radial, the meridional and azimuthal components are negligible. Assuming that the magnetic flux is conserved over spherical shells from the source surface to the planetary orbit, we calculate the decay of the magnetic field between the Source Surface and the orbit. In Fig 6, we plot the field value at the planetary orbit for each epoch of observations (including June 2007 and July 2008). The maximum value the field reaches at the planetary orbit can change by 100% between different epochs, which supports the importance of simultaneous observations when studying Star-Planet Interactions. We investigate the effect the error bars on the maps could have on the calculated magnetic field at the planetary orbit. To do so, for each epoch, we use as boundary condition each of the maps calculated for a range of $v \sin i$, $\Omega_{\rm eq}$, and $d\Omega$ (see Section 4.2), extrapolate the magnetic field for each map, and calculate the magnetic field at the position of the planet. We find that the mean difference between the field values presented in this paper and those calculated for the the maps

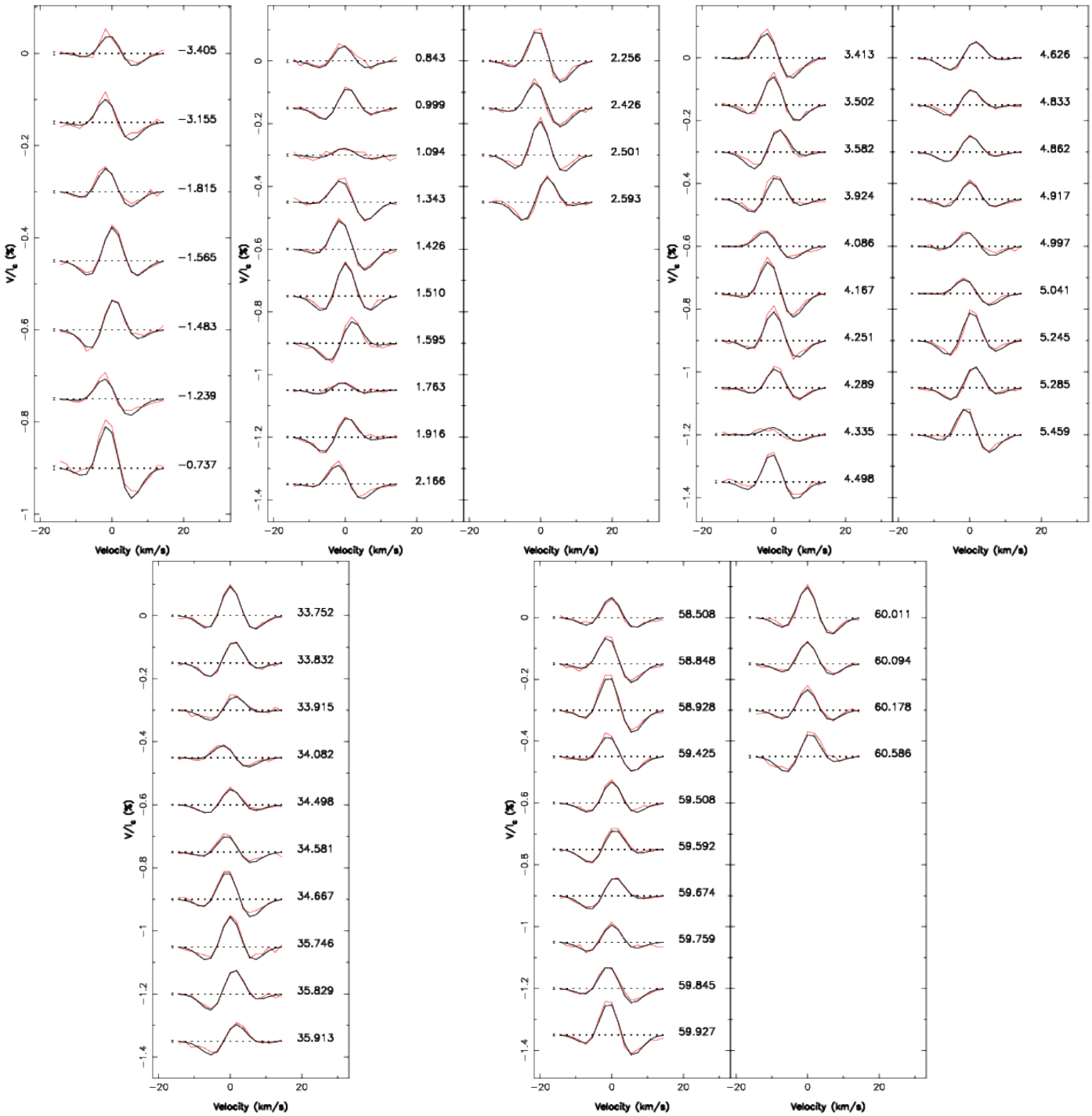

Figure 2. Observed Stokes V of HD189733 in red lines, and the fitted Stokes V profiles using ZDI in black, for June-July 2013 (top left), August 2013 (top middle), September 2013 (top right), September 2014 (bottom left) and July 2015 (bottom right). The rotational cycle of each observation (as listed in Table 2) and 1σ error bars are also shown next to each profile.

reconstructed for sets of $v \sin i$, $\Omega_{\rm eq}$, and $d\Omega$ is of the order of 3mG. The difference can reach up to 70% of the mean value over a small fraction of the orbit (for one epoch, all other epochs showed a smaller maximum difference value). This shows the robustness of our results: at the position of the planet, the variation of the stellar magnetic field is real and not affected by the error-bars on the maps.

5 DISCUSSION: MAGNETIC FIELD EVOLUTION

In this Section, we take advantage of previous spectropolarimetric observations of HD189733 to investigate the evolution of its magnetic field (intensity and topology) over a 9 year-timespan. The first reconstructed magnetic maps of HD189733, based on ESPaDOnS/CFHT data of June and August 2006, were presented by Moutou et al. (2007). Later

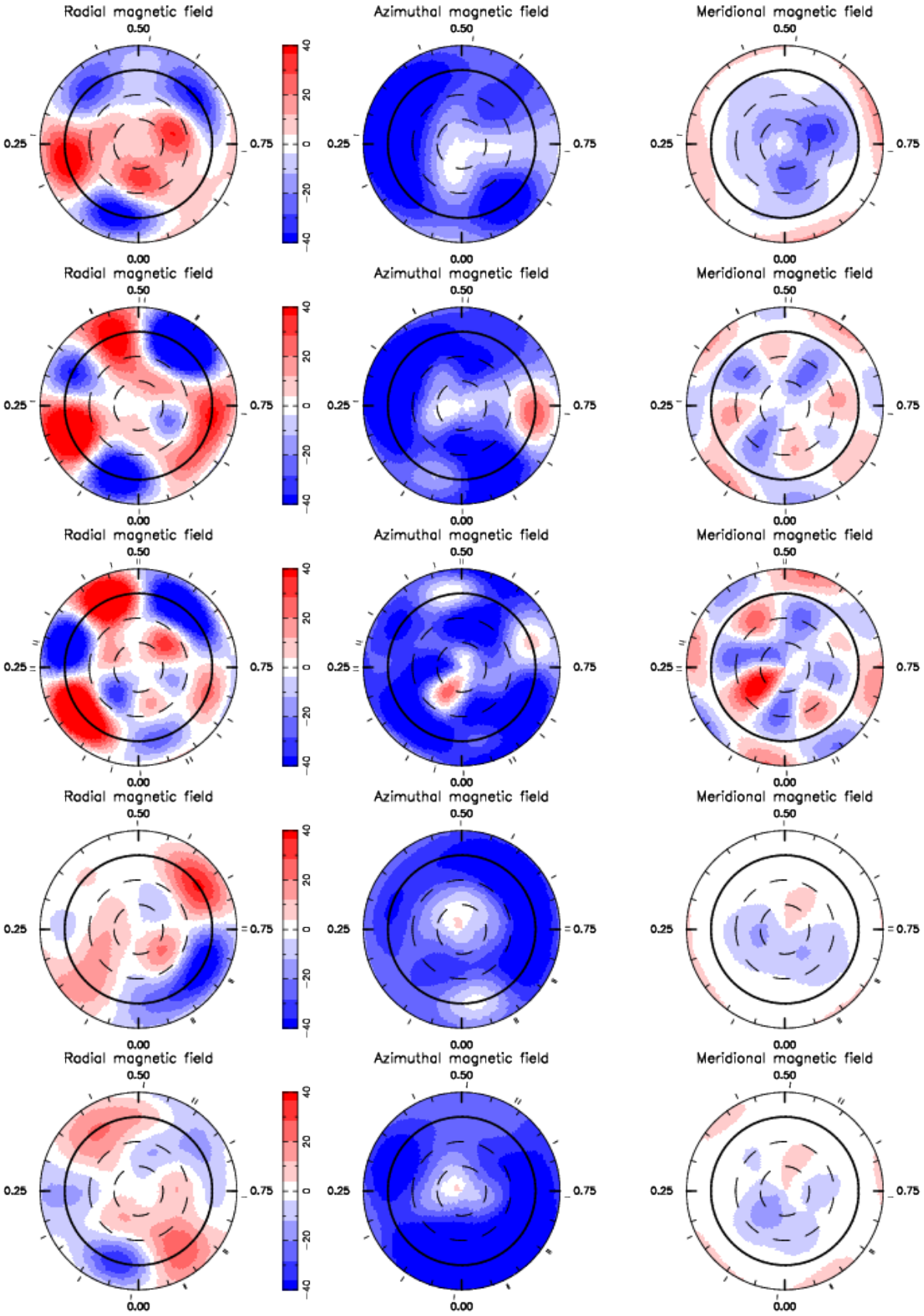

Figure 3. The reconstructed maps of HD 189733 for June-July 2013 (top row) August 2013 (second row), September 2013 (third row), September 2014 (fourth raw) and July 2015 (bottom row). The maps are in a polar flattened projection down to latitudes of −30°, the equator is represented by the bold circle. The radial, azimuthal and meridional field components are shown. The magnetic flux values are labelled in G. Radial ticks around each map indicate the rotational phase of our observations.

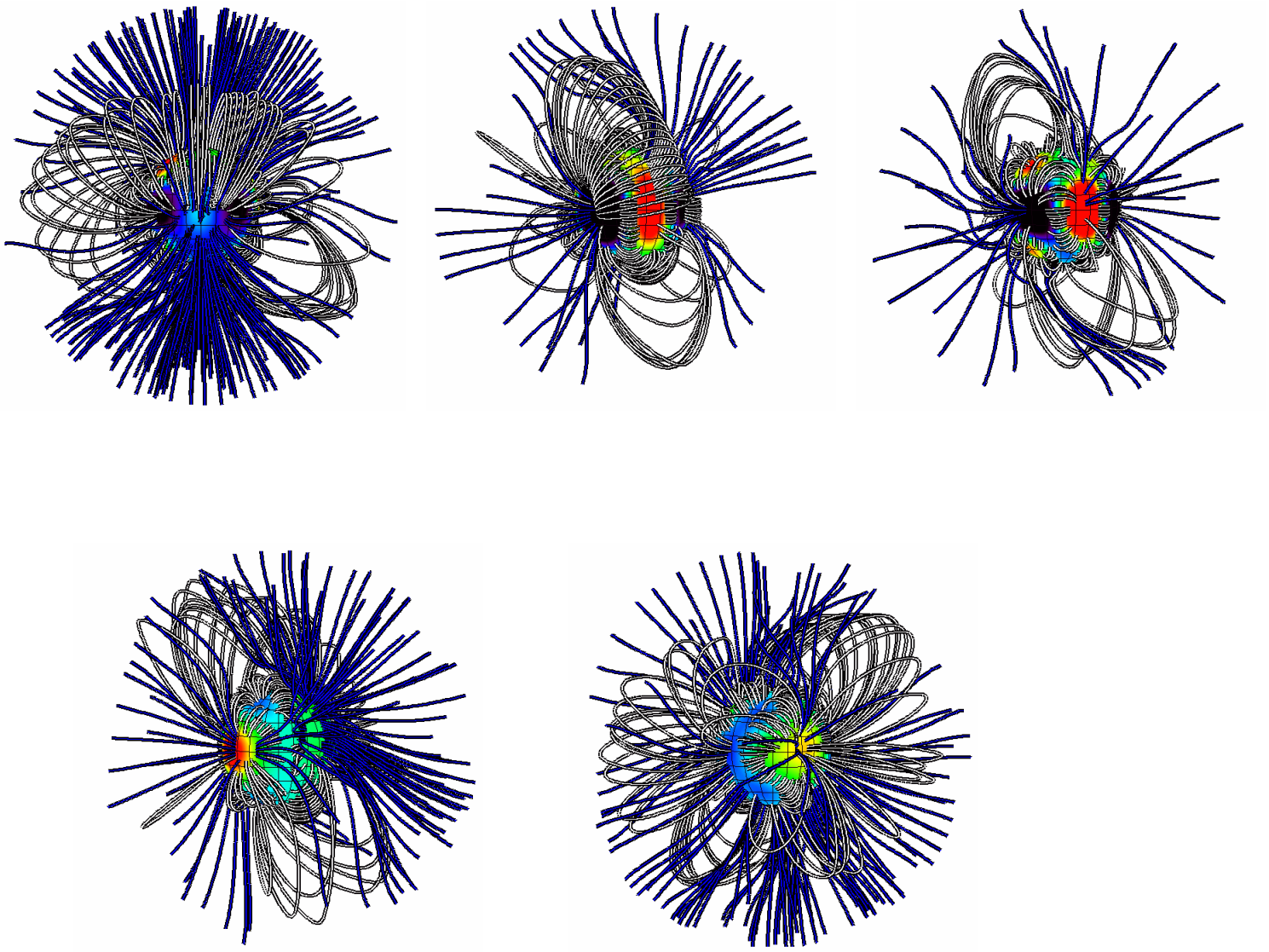

Figure 4. The extrapolated magnetic field of HD 189733 for June-July 2013 (top left), August 2013 (top middle), September 2013 (top right), September 2014 (bottom left) and July 2015 (bottom right). White lines correspond to the closed magnetic lines, blue ones to the open field lines (reaching the source surface). The star is shown at the same rotational phase (0.5) to better visualise the differences in magnetic field topology at each observing epoch. The star is viewed almost equator on ($\sim 5^{\circ}$), the inclination of the system on the sky (as seen from Earth).

on, and with the aim of detecting star-planet interaction signatures, Fares et al. (2010) presented two additional reconstructed magnetic maps of HD189733, based on spectropolarimetric observations of June 2007 and July 2008, as well as an update of the reconstructed map of 2006, merging June and August data as one dataset.

The data presented in this Paper (5 observing epochs spanning two years) shows that the field of HD 189733 can evolve over a few stellar rotations. Combining datasets spanning more than two stellar rotations systematically reduces the quality of the fit. Fares et al. (2010) have merged data obtained in 2006, spread over 5 stellar rotations. We revisited the summer 2006 data and found that the map was overfitted. We adopt the results of Moutou et al. (2007) in this paper.

Due to the 5-year gap in the observations, we can not investigate the presence of cyclic variations in the stellar magnetic field, in a similar way as those reported for the planet-hosting star τ Boo (Donati et al. 2008; Fares et al. 2009, 2013). Nevertheless, an evolution in the stellar magnetic field intensity and topology can be seen. Variations in both the axisymmetric contribution to the poloidal field

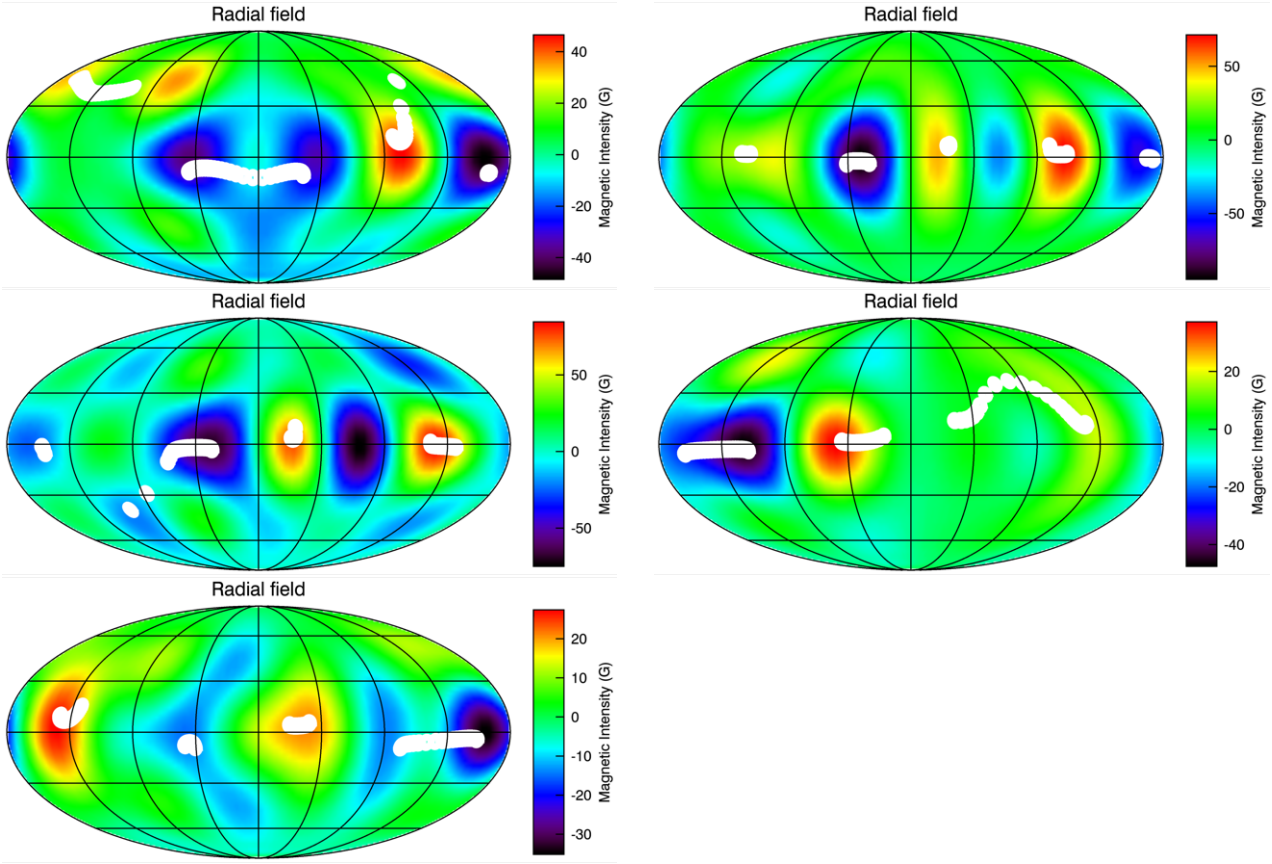

Figure 5. The radial magnetic field of HD 189733 for June-July 2013 (top left), August 2013 (top right), September 2013 (middle left), September 2014 (middle right) and July 2015 (bottom). White dots represent the footprints of the field lines connecting the stellar surface to the position of the planet on its orbit.

and the toroidal contribution to the total field are observed during this time span (see Fig 7).

For all epochs (apart from June 2006), the toroidal component dominates over the poloidal one. Petit et al. (2008) suggest, studying a sample of solar-like stars, that the toroidal energy dominates over the poloidal one for stars with rotation periods less than ~ 12 days. HD 189733, having an equatorial rotation period of 12 days, does not contradict their findings. On the other hand, Donati & Landstreet (2009) suggest that stars with Rossby number (Ro) < 1 develop toroidal fields. HD 189733 has a $Ro = 0.403$ (Vidotto et al. 2014). HD 189733 field's geometry is therefore compatible with the geometries observed for stars with similar masses and Ro numbers. The fraction of axisymmetric field is almost always less than 50%.

In addition, it is also interesting to compare the evolution of the stellar magnetic field within the 2013 data sets, that are separated by just 9 rotation periods. We note that little variation was seen for the toroidal component. The percentage of the contributors (dipole, quadrupole, octupole) to the poloidal field, on the other hand, has changed. The main contributor to the field (i.e. azimuthal component) does not change polarity. The radial component evolved, with negative and positive magnetic features appearing at the surface.

Table 4. Magnetic field characteristics of HD189733 for different epochs. The columns are: the epoch of the observations, the mean magnetic field at the surface of the star, the percentage of the toroidal energy relative to the total one, the percentage of the energy contained in the axisymmetric modes of the poloidal component relative to the poloidal energy, the percentage contribution of the dipolar, quadrupolar and octupolar components to the poloidal energy, and the mean stellar field at the position of the planetary orbit (see Section 4.3). Results of 2006 are from Moutou et al. (2007) and the results of 2007 and 2008 are from Fares et al. (2010). Error bars are calculated as in Mengel et al. (2016), i.e. by varying the input parameters within their error bars. The error bar on B_{orbit} is of the order of 3 mG (see text for more details).

Epoch	B_{mean} (G)	$E_{\rm tor}$ %	$E_{\rm axi}$ %	$E_{\rm l=1}$ %	$E_{\rm l=2}$ %	$E_{\rm l=3}$ %	B_{orbit} (mG)
7/2015	37^{+2}_{-2}	85^{+2}_{-2}	9^{+2}_{-2}	33^{+5}_{-2}	32^{+2}_{-4}	10^{+10}_{-1}	18
9/2014	32^{+2}_{-4}	78^{+3}_{-5}	10^{+2}_{-7}	21^{10}_{-6}	35^{+6}_{-2}	16^{+1}_{-6}	33
9/2013	42^{+2}_{-4}	59^{+1}_{-4}	2^{+2}_{-1}	4^{+4}_{-1}	3^{+2}_{-1}	49^{+2}_{-2}	31
8/2013	41^{+2}_{-5}	50^{+5}_{-5}	2_{-1}	10^{+5}_{-2}	20^{+5}_{-1}	32^{+3}_{-2}	39
6/2013	36^{+4}_{-3}	61^{+4}_{-3}	38^{+1}_{-2}	21^{+1}_{-1}	37^{+3}_{-3}	17^{+5}_{-1}	30
7/2008	36^{+1}_{-3}	77^{+3}_{-3}	17^{+2}_{-7}	30^{+4}_{-5}	26^{+2}_{-8}	12_{-2}	23
6/2007	22_{-3}	57^{+8}	26_{-5}	7^{+2}	33^{+7}	30^{+2}_{-1}	16
8/2006	20	60	10	35	20	13	
6/2006	18	35	52	50	36	12	

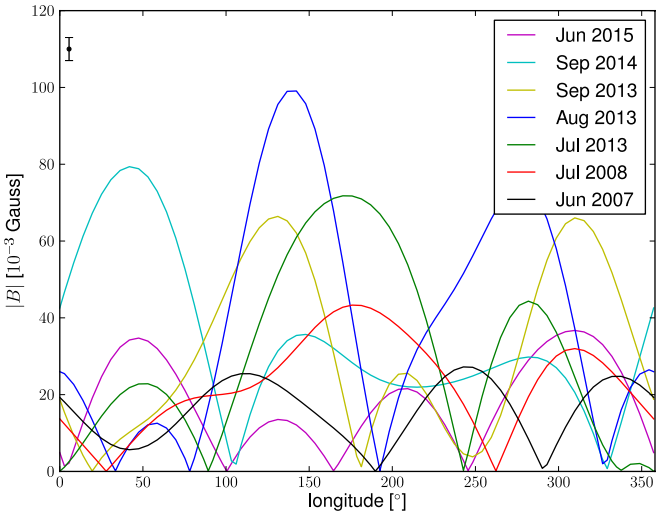

Figure 6. The stellar magnetic field value at the position of the planetary orbit (at 0.031 au). Different colours represent different epochs of observation. This plot shows that the planet is in a non-homogeneous environment, and that this environment varies from one epoch to the other. The error bar shown here is a mean error bar value per orbit, valid for all epochs (see text for more details).

6 CONCLUSIONS AND FUTURE PLANS

This paper is part of the MOVES collaboration (Multiwavelength Observations of an eVaporating Exoplanet and its Star), which aims to characterise comprehensively the complex environment of the exoplanet HD189733b. Orbiting a bright and active K dwarf at short distance, this transiting hot-Jupiter has been subjected to many stellar and planetary atmosphere studies. The main objectives of MOVES are to probe the different regions of the extended planetary atmosphere, its interactions with the host-star, and their temporal variability. The wider set of multi-wavelength observations (X-ray with Swift and XMM-Newton, UV spectroscopy with HST and XMM-Newton, and radio observations with LOFAR) were taken contemporaneously with the magnetic field mapping presented here.

In this first paper, we presented a detailed spectropolarimetric study of HD189733 and studied the evolution of its magnetism. Stellar magnetism is an important ingredient in stellar evolution, and also has important effects on planets surrounding these stars. The star was observed at five epochs (Jul 2013, Aug 2013, Sept 2013, Sept 2014 and Jun 2015), during which we also collected X-ray and UV observations (Wheatley et al, in prep). Using Zeeman Doppler Imaging, we reconstructed the magnetic maps of the star. With a strength up to 45 G, the magnetic field is dominated by the toroidal component at the five epochs. The toroidal component is mainly axisymmetric during all observing epochs. In contrast, the poloidal component is mainly non-axisymmetric. We will continue monitoring this system to study the magnetic evolution on time-scales longer than 2 years and look for a potential magnetic cycle. These reconstructed magnetic maps are crucial for analysing multi-wavelength observations. They allow us, modelling the stellar wind in the corona and at the planetary orbit, to reconstruct the X-ray emission and irradiation of the planet, as well as the spatial distribution of X-ray that will be absorbed by the extended atmosphere of the exoplanet.

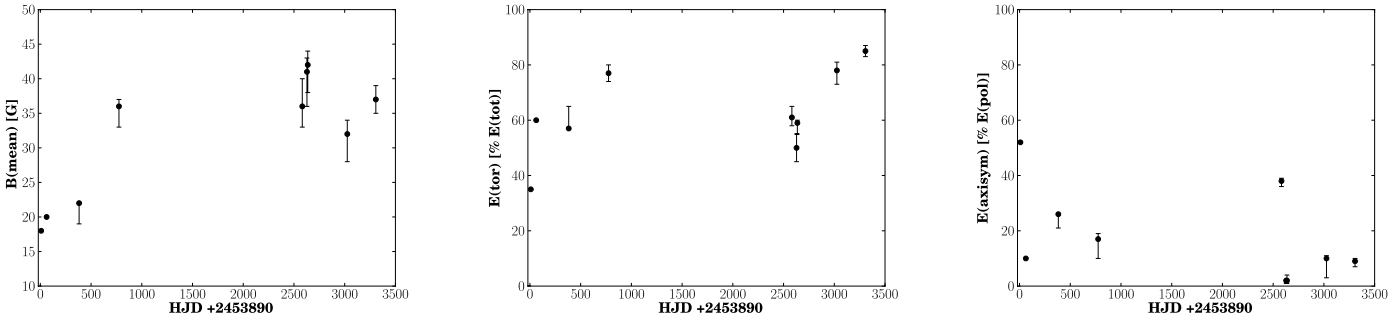

Figure 7. Magnetic field evolution of HD189733. From left to right: the square-root of the total magnetic energy, the toroidal energy relative to the total one, and the energy in the axisymmetric modes of the poloidal component relative to the energy of the poloidal component. Error bars are calculated as stated in the text.

ACKNOWLEDGMENTS

The authors thank an anonymous referee for their useful comments. This work is based on observations obtained with ESPaDOnS at the Canada-France-Hawaii Telescope (CFHT) and with NARVAL at the Télescope Bernard Lyot (TBL). CFHT/ESPaDOnS are operated by the National Research Council of Canada, the Institut National des Sciences de l'Univers of the Centre National de la Recherche Scientifique (INSU/CNRS) of France, and the University of Hawaii, while TBL/NARVAL are operated by INSU/CNRS. We thank the CFHT and TBL staff for their help during the observations, and in particular R. Cabanac and P. Petit. We also thank J.-F. Donati and E. Hébrard for useful comments on the data analysis. RF acknowledges financial support by WOW from INAF through the *Progetti Premiali* funding scheme of the Italian Ministry of Education, University, and Research. VB and AL acknowledge the support of the French Agence Nationale de la Recherche (ANR), under program ANR-12-BS05-0012 'Exo-Atmos'. Part of VB work has been carried out in the frame of the National Centre for Competence in Research "PlanetS" supported by the Swiss National Science Foundation (SNSF). V.B. also acknowledges the financial support of the SNSF. AAV acknowledges partial support from an Ambizione Fellowship of the Swiss National Science Foundation. ChH highlights financial support of the European Community under the FP7 by an ERC starting grant number 257431. P.W. is supported by a STFC consolidated grant (ST/L000733/7)

REFERENCES

Altschuler M. D., Newkirk G., 1969, Sol. Phys., 9, 131
Alvarado-Gómez J. D. et al., 2015, A&A, 582, A38
Augustson K. C., Brown B. P., Brun A. S., Miesch M. S., Toomre J., 2012, ApJ, 756, 169
Balona L. A., Abedigamba O. P., 2016, MNRAS, 461, 497
Barnes J. R., Collier Cameron A., Donati J.-F., James D. J., Marsden S. C., Petit P., 2005, MNRAS, 357, L1
Barnes J. R., Haswell C. A., Staab D., Anglada-Escudé G., 2016, MNRAS, 462, 1012
Ben-Jaffel L., Ballester G. E., 2013, A&A, 553, A52
Berdyugina S. V., Berdyugin A. V., Fluri D. M., Piirola V., 2011, ApJ, 728, L6
Boisse I., Moutou C., Vidal-Madjar A., Bouchy F., Pont F., Hébrard, 2009, A&A, 495, 959
Bott K., Bailey J., Kedziora-Chudczer L., Cotton D. V., Lucas P. W., Marshall J. P., Hough J. H., 2016, MNRAS, 459, L109
Bouchy F. et al., 2005, A&A, 444, L15
Bourrier V., Lecavelier des Etangs A., 2013, A&A, 557, A124
Bourrier V. et al., 2013, A&A, 551, A63
Brogi M., de Kok R. J., Albrecht S., Snellen I. A. G., Birkby J. L., Schwarz H., 2016, ApJ, 817, 106
Cegla H. M., Lovis C., Bourrier V., Beeck B., Watson C. A., Pepe F., 2016, A&A, 588, A127
Chandrasekhar S., 1961, Hydrodynamic and Hydromagnetic Stability. Clarendon Press, Oxford, U.K.
Cohen O., Kashyap V. L., Drake J. J., Sokolov I. V., Gombosi T. I., 2011, ApJ, 738, 166
Collier Cameron A., 2007, Astronomische Nachrichten, 328, 1030
Cuntz M., Saar S. H., Musielak Z. E., 2000, ApJ, 533, L151
Davis T. A., Wheatley P. J., 2009, MNRAS, 396, 1012
Distefano E., Lanzafame A. C., Lanza A. F., Messina S., Spada F., 2016, A&A, 591, A43
Donati J.-F. et al., 2006, MNRAS, 370, 629
Donati J.-F., Landstreet J. D., 2009, ARA&A, 47, 333

Donati J.-F. et al., 2008, MNRAS, 385, 1179
Donati J.-F., Semel M., Carter B. D., Rees D. E., Collier Cameron A., 1997, MNRAS, 291, 658
Ehrenreich D. et al., 2012, A&A, 547, A18
Fares R. et al., 2009, MNRAS, 398, 1383
Fares R. et al., 2010, MNRAS, 406, 409
Fares R., Moutou C., Donati J.-F., Catala C., Shkolnik E. L., Jardine M. M., Cameron A. C., Deleuil M., 2013, MNRAS, 435, 1451
Fossati L. et al., 2010, ApJ, 714, L222
Grießmeier J.-M., Preusse S., Khodachenko M., Motschmann U., Mann G., Rucker H. O., 2007, Planet. Space Sci., 55, 618
Grießmeier J.-M., Zarka P., Spreeuw H., 2007, A&A, 475, 359
Helling C., Jardine M., Diver D., Witte S., 2013, Planet. Space Sci., 77, 152
Ip W.-H., Kopp A., Hu J.-H., 2004, ApJ, 602, L53
Jackson A. P., Davis T. A., Wheatley P. J., 2012, MNRAS, 422, 2024
Jardine M., Cameron A. C., 2008, A&A, 490, 843
Jardine M., Collier Cameron A., Donati J.-F., 2002, MNRAS, 333, 339
Koskinen T. T., Harris M. J., Yelle R. V., Lavvas P., 2013, Icarus, 226, 1678
Lammer H. et al., 2011, Origins of Life and Evolution of the Biosphere, 41, 503
Lecavelier Des Etangs A., 2007, A&A, 461, 1185
Lecavelier des Etangs A. et al., 2012, A&A, 543, L4
Lecavelier Des Etangs A. et al., 2010, A&A, 514, A72
Lecavelier Des Etangs A., Sirothia S. K., Gopal-Krishna, Zarka P., 2011, A&A, 533, A50
Llama J., Vidotto A. A., Jardine M., Wood K., Fares R., Gombosi T. I., 2013, MNRAS, 436, 2179
Louden T., Wheatley P. J., 2015, ApJ, 814, L24
Matsakos T., Uribe A., Königl A., 2015, A&A, 578, A6
Mengel M. W. et al., 2016, MNRAS, 459, 4325
Mengel M. W. et al., 2017, MNRAS, 465, 2734
Morin J. et al., 2008a, MNRAS, 390, 567
Morin J. et al., 2008b, MNRAS, 390, 567
Moutou C. et al., 2007, A&A, 473, 651
Murray-Clay R. A., Chiang E. I., Murray N., 2009, ApJ, 693, 23
Petit P. et al., 2008, MNRAS, 388, 80
Pillitteri I., Wolk S. J., Cohen O., Kashyap V., Knutson H., Lisse C. M., Henry G. W., 2010, ApJ, 722, 1216
Poppenhaeger K., Schmitt J. H. M. M., Wolk S. J., 2013, ApJ, 773, 62
Preusse S., Kopp A., Büchner J., Motschmann U., 2005, A&A, 434, 1191
Reiners A., 2006, A&A, 446, 267
Reiners A., 2012, Living Reviews in Solar Physics, 9, 1
Reiners A., Schmitt J. H. M. M., 2002, A&A, 384, 155
Reinhold T., Reiners A., Basri G., 2013, A&A, 560, A4
Riley P., Linker J. A., Mikić Z., Lionello R., Ledvina S. A., Luhmann J. G., 2006, ApJ, 653, 1510
Rimmer P. B., Helling C., 2013, ApJ, 774, 108
Rimmer P. B., Helling C., Bilger C., 2014, International Journal of Astrobiology, 13, 173
Rimmer P. B., Stark C. R., Helling C., 2014, ApJ, 787, L25
Scandariato G. et al., 2013, A&A, 552, A7
See V., Jardine M., Fares R., Donati J.-F., Moutou C., 2015, MNRAS, 450, 4323
Shkolnik E., Bohlender D. A., Walker G. A. H., Collier Cameron A., 2008, ApJ, 676, 628
Shkolnik E., Walker G. A. H., Bohlender D. A., 2003, ApJ, 597, 1092
Shulyak D., Reiners A., Seemann U., Kochukhov O., Piskunov N., 2014, A&A, 563, A35
Smith A. M. S., Collier Cameron A., Greaves J., Jardine M., Langston G., Backer D., 2009, MNRAS, 395, 335
Triaud A. H. M. J. et al., 2009, A&A, 506, 377
van Ballegooijen A. A., Nisenson P., Noyes R. W., Löfdahl M. G., Stein R. F., Nordlund Å., Krishnakumar V., 1998, ApJ, 509, 435
Vidal-Madjar A., Lecavelier des Etangs A., Désert J.-M., Ballester G. E., Ferlet R., Hébrard G., Mayor M., 2003, Nature, 422, 143
Vidotto A. A., Fares R., Jardine M., Donati J.-F., Opher M., Moutou C., Catala C., Gombosi T. I., 2012, MNRAS, 423, 3285
Vidotto A. A., Fares R., Jardine M., Moutou C., Donati J.-F., 2015, MNRAS, 449, 4117
Vidotto A. A. et al., 2014, MNRAS, 441, 2361
Vidotto A. A., Jardine M., Helling C., 2010, ApJ, 722, L168
Vidotto A. A., Opher M., Jatenco-Pereira V., Gombosi T. I., 2009, ApJ, 703, 1734
Winn J. N. et al., 2007, AJ, 133, 1828
Winn J. N. et al., 2006, ApJ, 653, L69
Zarka P., 2007, Planet. Space Sci., 55, 598